

## Spectra of $L$ x rays from fast highly charged Xe ions traveling in solids

V. Horvat, R. L. Watson, and R. Parameswaran

Cyclotron Institute and Department of Chemistry, Texas A&M University, College Station, Texas 77843

(Received 6 June 1994)

Spectra of  $L$  x rays emitted by 6- and 8-MeV/u Xe ions interacting with a variety of solid targets have been measured with a curved-crystal spectrometer. The spectra displayed an overall structure consisting of six strong peaks which were fairly well resolved for low- $Z$  targets ( $Z_2 = 3-6$ ), but broadened into two featureless groups for higher- $Z$  targets. The main components were identified as  $L\alpha_1$  and  $L\beta_1$  pairs associated with initial-state configurations having one to six  $L$ -shell vacancies. Detailed spectral analysis provided estimates of the average projectile charges and the average  $L$ - and  $M$ -electron populations *inside* the solids.

PACS number(s): 34.50.Fa, 32.30.Rj

### I. INTRODUCTION

The interaction of fast heavy ions with matter has been under investigation since the early days of atomic physics. Interest in this subject originates not only from a desire to understand the fundamental collision processes involved, but also from practical considerations related, for instance, to the determination of stopping power, the assessment of radiation damage, and the development of techniques for materials modification and analysis.

One of the most useful methods for studying the interaction of fast heavy ions with atoms in a solid-state environment is x-ray emission spectroscopy. The principal reasons for this are that x-rays are state specific, they can be observed from depths well below the surface without energy degradation, and their relative intensities are modified by absorption in a well-known and usually correctable manner. Information concerning the states of fast ions traveling in solids is provided directly by the x rays emitted from the projectiles themselves and indirectly by the x rays emitted from the target atoms.

Many studies of projectile  $K$  x-ray emission in thick targets have been performed over the past two decades using different combinations of target and projectile atomic numbers. These measurements have concentrated on projectiles with atomic number up to 18 and energies up to several MeV/u (see, for example, Refs. [1-6]). The methods used have included varying the target thickness [7-11] and composition [12], as well as comparing spectra produced in solid and gas targets [13,14]. It has also been demonstrated that thin target spectra can be influenced by the initial projectile charge [15-17]. Investigations of  $L$  x-ray emission in fast ion collisions have been carried out for a number of systems [18-26]. Of particular relevance to the present work are the studies of Hagmann *et al.* [25,26] in which  $L$  x-ray emission from 0.05 to 0.35 MeV/u iodine ions passing through (thin) solid targets ranging in atomic number from 47 to 92 was examined. Ionization cross sections deduced from the x-ray yields were discussed in terms of a molecular-orbital model and an oscillatory behavior of the  $L\beta$ -to- $L\alpha$  intensity ratio as a function of target atomic number (previ-

ously observed by Datz *et al.* [24]) was interpreted by considering the conditions required for electron promotion via specific molecular-orbital excitations. At these relatively low projectile velocities where  $L$ -vacancy-producing collisions are rare, it was found that the average charges of iodine ions deduced from the  $L$  x-ray energy shifts were considerably higher than the average equilibrium charges.

It is well established that as a high-velocity ion penetrates the surface of a solid, it rapidly loses those electrons whose orbital velocities  $v_e$  are lower than the ion velocity  $v_i$  while its inner-shell electrons occasionally undergo excitation or ionization [27]. Typical time intervals between collisions are much shorter than the lifetimes of inner-shell vacancies and so the projectile x-ray spectrum reflects the distribution of states attained after a series of subsequent collisions. As a consequence of the distribution of x-ray emitting states produced and the associated multiplet structure, the resulting spectra generally contain a multitude of closely spaced lines [28]. A variety of line shifting and peak broadening mechanisms can add to the complexity of the spectra [4,29-32]. Consequently, in many cases, it is not possible to resolve the individual x-ray lines even with the highest resolution attainable.

The present paper describes a study of the spectra of  $L$  x rays emitted by 6- and 8-MeV/u Xe projectiles traveling in thick and thin solid targets. At these velocities, the equilibrium charges of Xe (after emerging from a solid) are in the range of  $43+$  to  $45+$ . In the ground state of  $Xe^{44+}$ , electrons completely fill the  $K$  and the  $L$  shell, while the remaining shells are empty. However, the charge state equilibration process is a dynamic one in which there is a constant exchange of electrons between the ion and the medium. In the cases under consideration here, excitation or ionization of  $K$ -shell electrons is extremely rare, as is electron capture to shells higher than the  $M$  shell. Therefore, the electronic configurations contributing to the equilibrium charge state distribution are expected to primarily consist of those formed from the ground-state configuration by the removal of  $L$ -shell electrons and the addition of  $M$  shell electrons. The ob-

ject of the work described herein was to examine the  $L$  x ray structure under moderately high resolution and identify the major x ray components. This information was then used to deduce the average  $L$ - and  $M$ -shell electron population distributions of Xe ions *inside the solid*.

## II. EXPERIMENTAL METHODS

Beams of 6-MeV/u Xe<sup>17+</sup> and 8-MeV/u Xe<sup>21+</sup> were extracted from the Texas A&M K-500 superconducting cyclotron, charge analyzed, and optically focused on a Zn-CdS phosphor with the aid of a closed-circuit television camera. The beam was collimated by the 2-mm-diam target cell entrance aperture and a separate 3-mm-diam collimator located 5 cm upstream from the target cell. The beam intensity was monitored by measuring the current from the front collimator, the current from the target cell, and/or the current from a Faraday cup placed directly behind the target cell, depending on the target thickness and its electrical conductivity.

The targets consisted of the following: (a) thick (~2 mm) pressed pellets made from powders of pure B, BN, C, NaF, KCl, and the oxides of Ca, Sc, Cr, and Mn; (b) a 0.024-mm-thick Be wafer; (c) a thick slice of Li metal; (d) thick sheets (~0.13 mm) of Al, Ti, and V; (e) thin foils of C (100 and 200  $\mu\text{g}/\text{cm}^2$ ), Al (150  $\mu\text{g}/\text{cm}^2$ ), and Ni (180  $\mu\text{g}/\text{cm}^2$ ). They were oriented at 45° with respect to the (horizontal) beam direction and at 45° with respect to the (vertical) spectrometer axis such that the spectrometer viewed them from the front.

A 12.7-cm Johansson-type curved-crystal x ray spectrometer with the focal circle oriented perpendicular to the beam axis was used to measure the x ray spectra. X rays diffracted from a LiF crystal were counted by a flow proportional counter [1 atm of argon (90%) and methane (10%)] having a 65- $\mu\text{g}/\text{cm}^2$ -thick stretched polypropylene window. The spectrometer's view of the interaction region was defined by a 1.6-mm-diam aperture located at the top of the target cell. Other details concerning the spectrometer and the electronic apparatus have been described elsewhere [33]. The crystal angle and focal circle position were adjusted to give maximum diffraction intensities of Ca and Mn  $K\alpha_{1,2}$  x rays, respectively. It was verified that no energy shifts occurred when the targets were changed. Energy calibration of the spectrometer was performed using the measured diffraction positions of the  $K\alpha_{1,2}$  and  $K\beta_1$  peaks of K, Ca, Sc, Ti, V, Cr, and Mn.

Data acquisition was accomplished by means of a Nucleus PC Analyzer card with the accompanying software [34], installed on an IBM XT computer and operated in the multiscaler mode. The collected data were stored on a floppy disk. Data analysis was carried out off-line with a 486 PC-AT along with FORTRAN least-squares-fitting programs written specifically for this purpose.

Spectra recorded during the bombardment of a pellet containing Ca and Mn oxides by 6-MeV/u Xe<sup>17+</sup> and 8-MeV/u Xe<sup>21+</sup> ions are shown in Figs. 1(a) and 1(b), respectively. The spectra contain structures produced by  $K$  x rays from Ca (labeled  $A$ ,  $B$ , and  $C$ ),  $L$  x rays from

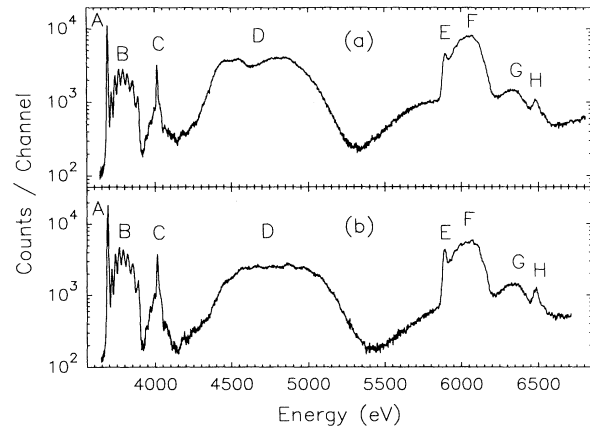


FIG. 1. Spectrum of target  $K$  x rays and projectile  $L$  x rays emitted during the bombardment of a compressed pellet of Ca and Mn oxides with (a) 6-MeV/u Xe ions and (b) 8-MeV/u Xe ions. The peak labels are explained in the text.

Xe ( $D$ ), and  $K$  x rays from Mn ( $E$ ,  $F$ ,  $G$ , and  $H$ ). The Ca and Mn  $K\alpha_{1,2}$  peaks ( $A$  and  $E$ ) and  $K\beta_1$  peaks ( $C$  and  $H$ ) display large enhancements arising from photoionization by the high flux of x rays having energies greater than the  $K$  binding energies. The structures  $B$  and  $F$  are due to Ca and Mn  $K\alpha$  x ray satellites (i.e.,  $K$  x ray transitions in atoms with  $L$ -shell spectator vacancies in addition to the single  $K$  vacancy involved in the transition). The resolution of the spectrometer was sufficient to resolve the complete set of seven Ca  $K\alpha$  satellites. The  $K\alpha$  satellite lines of Mn are not resolved, although their separation is larger, due to the rapid deterioration of the spectrometer resolution with decreasing Bragg angle. The structure marked  $G$  is due to the Mn  $K\alpha$  x ray hypersatellites, which originate from transitions in atoms having empty  $K$  shells and zero to seven vacancies in the  $L$  shell. The hypersatellite distribution of Ca overlaps the much stronger  $K\beta_1$  peak. For both Ca and Mn, the energies of the  $K\beta$  satellites and hypersatellites are above the  $K$  absorption edge. Therefore, these x rays are strongly absorbed within the target and the corresponding peaks are greatly suppressed in the spectra.

It can be seen from Fig. 1 that the intensity of Xe  $L$  x rays is comparable to the intensities of the Ca and Mn  $K$  x rays. The various  $L$  x ray components are not resolved in this spectrum, but it is clear that the overall spectral shape and position changes when the projectile energy increases from 6 to 8 MeV/u. The structure of the Xe  $L$  x ray spectrum was found to exhibit a strong dependence on the target atomic number ( $Z_2$ ), as demonstrated in Fig. 2, where spectra obtained with targets having  $Z_2$  from 25 down to 3 are compared. It is evident that partially resolved components emerge as  $Z_2$  decreases. Similar behavior was observed in the thin target measurements, as shown in Fig. 3. Additional measurements

were performed with a variety of carbon targets to investigate the effects of target thickness and beam energy. These spectra are shown in Fig. 4.

Small deviations from a  $90^\circ$  viewing angle can result in significant Doppler shifts at the projectile velocities employed in the present experiments. The spectrometer was oriented vertically with its focal plane perpendicular to the beam direction in order to minimize this problem and was configured in such a way that it could be rotated about a vertical axis through the centers of the target and the diffracting crystal (see [33]). By measuring spectra at different rotation angles, it was possible to check for

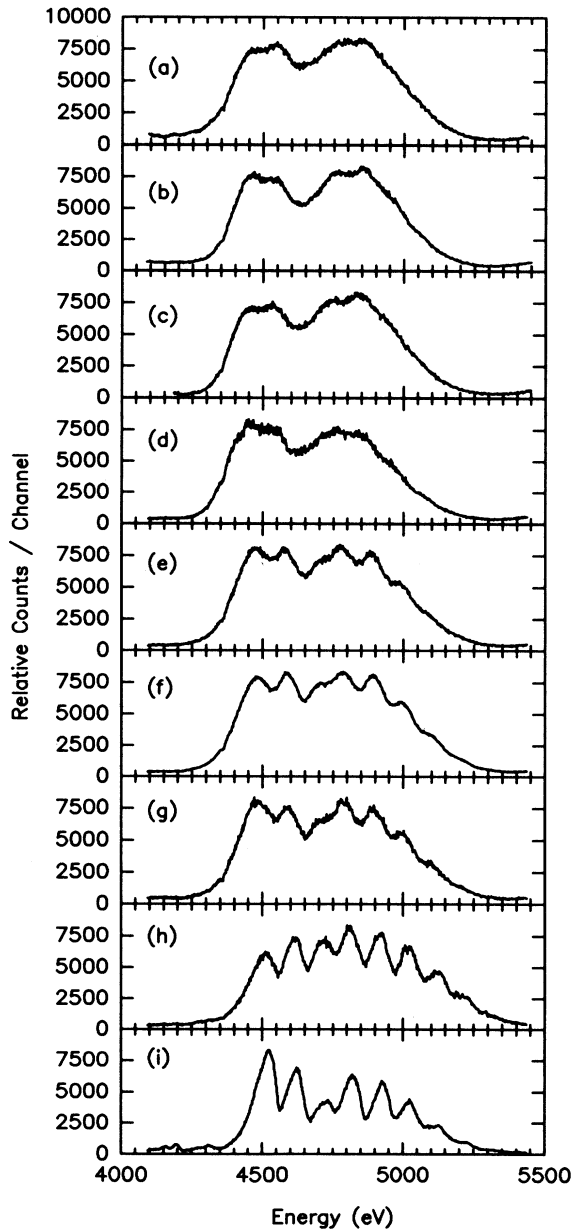


FIG. 2. Spectra of Xe L x rays emitted by 6-MeV/u Xe ions traveling in thick targets of (a) CaO+MnO, (b) KCl, (c) Al, (d) NaF, (e) BN, (f) C, (g) B, (h) Be, and (i) Li.

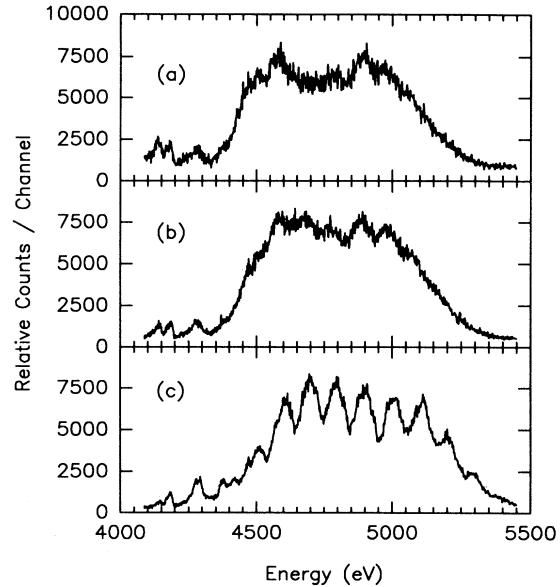


FIG. 3. Spectra of Xe L x rays emitted by 8-MeV/u Xe ions passing through thin, self-supporting targets of (a)  $180\text{-}\mu\text{g}/\text{cm}^2$  Ni, (b)  $150\text{-}\mu\text{g}/\text{cm}^2$  Al, and (c)  $200\text{-}\mu\text{g}/\text{cm}^2$  C.

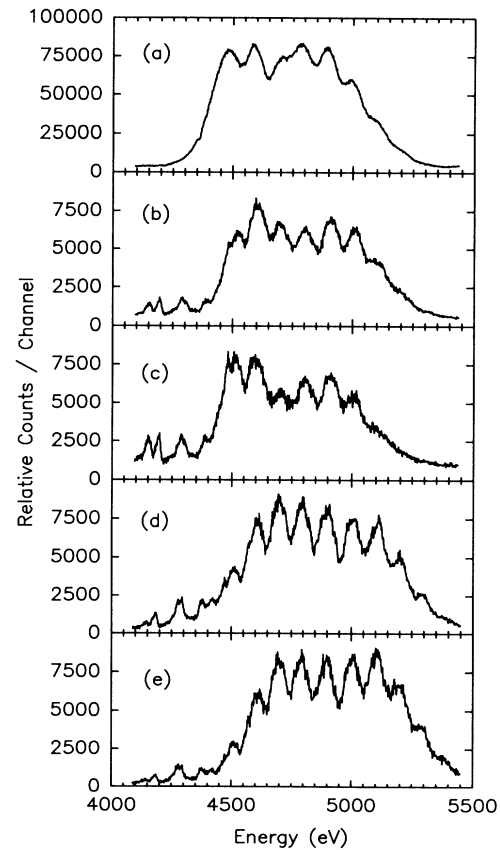


FIG. 4. Comparison of Xe L x-ray spectra obtained with the following projectile-target combinations: (a) 6-MeV/u Xe-thick C pellet, (b) 6-MeV/u Xe- $200\text{-}\mu\text{g}/\text{cm}^2$  C foil, (c) 6-MeV/u Xe- $100\text{-}\mu\text{g}/\text{cm}^2$  C foil, (d) 8-MeV/u Xe- $200\text{-}\mu\text{g}/\text{cm}^2$  C foil, and (e) 8-MeV/u Xe- $200\text{-}\mu\text{g}/\text{cm}^2$  C foil preceded by a  $200\text{-}\mu\text{g}/\text{cm}^2$  C stripper foil.

Doppler shifts. These measurements showed that the lines contributing to the Xe  $L$  x ray spectra were Doppler shifted by less than 1 eV.

### III. INTERPRETATION OF THE SPECTRA

#### A. General observations

The range of (6–8)-MeV/u Xe ions in solids with atomic numbers between 3 and 25 is of the order of 20 mg/cm<sup>2</sup> (0.1 mm) [35]. All the thick targets used in this experiment were much thicker than this, which means that the beam particles were completely stopped. The charge changes very rapidly from its initial value reaching around 44+ (the average equilibrium charge) within the first 150–200  $\mu\text{g}/\text{cm}^2$  [36]. Thereafter, the average charge decreases gradually as the ion slows down. By the time the projectile has lost 1 MeV/u, the average charge has dropped approximately one unit [36]. The total distance traveled at this point is about 2 mg/cm<sup>2</sup> (10  $\mu\text{m}$ ), which is 10% of the full range. Since the number of possible electronic configurations involving  $L$  vacancies is quite large for each contributing charge state, the resulting  $L$  x ray spectrum was expected to contain many closely spaced lines covering a wide energy range. Therefore, the structure displayed by the spectra for the low- $Z$  targets (see Fig. 1) is, at first sight, rather surprising.

The spectra indicate that the observed x rays originate from Xe ions having a fairly restricted range of charges. This deduction is based on the following two spectral characteristics. (a) The observed  $L$  x ray structure begins around 4.4 keV, whereas the most prominent  $L$  x ray line ( $L\alpha_1$ ) from singly ionized Xe atoms has an energy of 4.1 keV [37]. This large energy shift means (as will be demonstrated later) that only ions stripped of most of their outer electrons (down to the  $L$  shell) contribute to the spectra. (b) The attenuation lengths of Xe  $L$  x rays vary widely over the range of target  $Z$  examined and yet the overall positions and widths of the  $L$  x ray distributions do not change very much (see Fig. 2). For example, in KCl the thickness required to attenuate 4.5-keV x rays by 90% is 4.6 mg/cm<sup>2</sup> [38], while the range of 6-MeV/u Xe ions in KCl is about 14 mg/cm<sup>2</sup>. On the other hand, for Li the 90% attenuation thickness is 0.92 g/cm<sup>2</sup> and the range is 10 mg/cm<sup>2</sup>. Hence, if  $L$  x ray emission from Xe ions having low charges (i.e., near the end of their

range) was very probable, the Li spectrum would extend to much lower energies than the KCl spectrum. As may be discerned from Fig. 2, this is clearly not the case.

The spectra from thin targets, shown in Fig. 4, provide further insight regarding the contributing charge states. The charge equilibration thickness for 6–8-MeV/u Xe is approximately 200  $\mu\text{g}/\text{cm}^2$ . Therefore, the only charge states that can make significant contributions to the spectra shown in Figs. 4(b)–4(d) are between the incident charge (17+ and 21+) and the equilibrium charge (43+ and 45+). A rough estimate of the mean depth within a carbon target at which an  $L$  vacancy is produced in the projectile may be obtained by assuming a geometric  $L$ -shell ionization cross section ( $\sim 5 \times 10^{-19}$  cm<sup>2</sup>). This gives a mean depth  $\sim 2 \times 10^{-5}$  cm and since the nominal lifetime of an  $L$  vacancy in a singly ionized Xe atom is about  $2 \times 10^{-16}$  s [39], the expected decay length is only of the order of  $7 \times 10^{-7}$  cm. Therefore it may be concluded that most of the  $L$  x rays are emitted while the projectile is still inside a 100- $\mu\text{g}/\text{cm}^2$  carbon target (which has a linear thickness of  $4.4 \times 10^{-5}$  cm). The spectra for 6-MeV/u Xe on 200- and 100- $\mu\text{g}/\text{cm}^2$  C targets are very similar, with the thinner target yielding slightly less contribution from the highest charge states than the thicker one. The absence from these spectra of low charge state components indicates that  $L$  x ray emission during the early stages of the charge equilibration process is not very probable. Surprisingly, the spectrum obtained with a thick target [Fig. 4(a)] is not dramatically different from the spectra obtained with thin targets, although it does display a somewhat higher intensity of  $L$  x rays from lower charge states in the region of 4300–4500 eV. These x rays from the lower charge states must be produced beyond the equilibration depth, after the ions have lost several MeV/u.

Comparing the spectra obtained with 6- and 8-MeV/u projectiles passing through the 200- $\mu\text{g}/\text{cm}^2$  target [Figs. 4(b) and 4(d)], it may be seen that the latter displays components from higher charge states than the former and it also contains less intensity in the lowest charge state components. This is exactly the behavior expected since the equilibrium charge distributions at these two energies are displaced from each other by about two charge units. The effect of prestripping the 8-MeV/u beam by placing a 200- $\mu\text{g}/\text{cm}^2$  C foil 3 cm upstream from the target may be seen by comparing Figs. 4(d) and 4(e). The stripped ions

TABLE I. Apparent Xe  $L$  x-ray peak energies and average widths (both in eV).

Target	Projectile energy (MeV/u)	Peak number								FWHM	
		1	2	3	4	5	6	7	8		9
Li	6	4447	4517	4619	4723	4818	4924	5024	5119	5210	74.6
Be	6	4421	4505	4611	4715	4811	4916	5021	5123	5219	85.2
B	6	4380	4474	4585	4697	4790	4897	5003	5107	5207	105.3
C	6	4371	4468	4583	4695	4788	4895	5002	5107	5212	108.8
NaF	6	4367	4440	4545	4659	4752	4853	4958	5064	5163	117.8
C <sup>a</sup>	6	4496	4600	4701	4803	4909	5012	5109	5203	5295	92.5
C <sup>a</sup>	8	4503	4601	4699	4796	4898	5005	5106	5201	5296	80.8

<sup>a</sup>Target thickness of 200  $\mu\text{g}/\text{cm}^2$ .

are expected to have a charge distribution centered about an average charge that is somewhat higher than the equilibrium charge inside the target due to Auger decay after emerging from the stripping foil. Although the spectrum obtained with the stripped beam displays slightly enhanced high-energy x ray components, it is very similar to the spectrum obtained with the unstripped beam. This fact reaffirms the conclusion reached above, namely, that the spectra obtained with thin targets primarily reflect charge states close to those attained at equilibrium and they contain little contribution from the lower charge states that evolve on the way to equilibrium.

As a means of comparing the spectra more quantitatively, least-squares fits were performed using nine Gaussian peaks to represent the gross structural features. The quality of the fit was excellent in all cases. The resulting peak centroid energies and average widths [full width at half maximum (FWHM)] are listed in Table I for a few of the spectra obtained with thick and thin targets. It may be seen from this table that, for the thick targets, the peak energies decrease linearly with increasing  $Z_2$ . As is evident in Fig. 2, the relatively well resolved components appearing in the spectrum obtained with the lithium target broaden with increasing target atomic number and almost completely blend together at  $Z_2=10$  (NaF). The average width of a peak in the spectrum obtained with a Li target is about a factor of 4.5 larger than the spectrometer resolution (17.4 eV) and so even the peaks in this spectrum are broadened. The average peak widths listed in Table I indicate that the broadening effect increases rapidly from Li to B and then levels off to a much slower rate of increase thereafter. It should also be noted that the average peak width in the spectrum obtained with a thin carbon target (at 6 MeV/u) is 15% smaller than that for a thick carbon target. Peak broadening has been observed previously in studies of  $K$  x-ray emission from low- $Z$  ions traveling in solids at energies up to several MeV/u [4,30,31]. Among the possible causes considered were the following: (a) Heisenberg broadening due to the short collision times, (b) modulation of electron binding and transition energies caused by interactions with the electrons and nuclei of the target, and (c) photon wave-packet perturbation via elastic scattering of target valence electrons by the moving ion [40]. However, in all the studies referenced above, the observed peak widths were substantially larger than those predicted on the basis of these mechanisms. In the present case, variation in the number of  $M$ -shell electrons present at the time of  $L$  x ray emission was expected to be a major contributor of the observed broadening effect, as will be discussed further in Sec. III C.

#### B. Analysis of the $L$ x-ray structure

In order to predict the underlying  $L$  x-ray structure contained in the measured spectra, the energies of transitions to the  $L$  shell within the energy region viewed were calculated using the multiconfigurational Dirac-Fock program of Desclaux [41]. These calculations were performed for all initial-state configurations containing two  $K$  shell electrons plus  $n_L$   $L$ -shell electrons plus one  $M$ -shell electron, where  $n_L$  ranged from 7 to 0.

Configurations for all possible combinations of the occupation numbers  $n_{L_1}$ ,  $n_{L_2}$ , and  $n_{L_3}$  of the  $L_1$ ,  $L_2$ , and  $L_3$  subshells were included. The specific transitions considered were  $Ll(M_1 \rightarrow L_3)$ ,  $L\alpha_{1,2}(M_{4,5} \rightarrow L_3)$ ,  $L\eta(M_1 \rightarrow L_2)$ ,  $L\beta_1(M_4 \rightarrow L_2)$ ,  $L\beta_4(M_2 \rightarrow L_1)$ , and  $L\beta_3(M_3 \rightarrow L_1)$ . The energies obtained for the  $L\alpha_1$  and  $L\beta_1$  transitions are listed in Table II.

A simulated spectrum was constructed for each value of  $n_L$  by assuming a statistical population of initial states and using Scofield's [42] calculated  $L$ -shell transition

TABLE II. Initial-state occupation numbers ( $n_{L_i}$ ) of the  $L_1$ ,  $L_2$ , and  $L_3$  subshells,  $L\alpha_1$  and  $L\beta_1$  transition energies (in eV) with zero spectator electrons in the  $M$  shell, and relative statistical population probabilities ( $P_{n_L}$ ) for Xe ions.

$n_{L_1}$	$n_{L_2}$	$n_{L_3}$	$E(L\alpha_1)$	$E(L\beta_1)$	$P_{n_L}$
0	0	0	5213.4	5551.3	1
1	0	0	5137.9	5472.1	1/4
0	1	0	5106.9	5418.9	1/4
0	0	1	5104.2	5445.2	2/4
2	0	0	5062.4	5393.0	1/28
1	1	0	5031.6	5340.3	4/28
1	0	1	5028.9	5366.2	8/28
0	2	0	5001.1		1/28
0	1	1	4998.4	5313.8	8/28
0	0	2	4995.8	5339.8	6/28
2	1	0	4956.2	5261.6	1/28
2	0	1	4953.7	5287.2	2/28
1	2	0	4925.9		1/28
1	1	1	4923.3	5235.2	8/28
1	0	2	4920.7	5260.9	6/28
0	2	1	4893.3		2/28
0	1	2	4890.6	5209.2	6/28
0	0	3	4888.1	5234.9	2/28
2	2	0	4850.7		1/70
2	1	1	4848.1	5156.7	8/70
2	0	2	4845.7	5182.0	6/70
1	2	1	4818.3		8/70
1	1	2	4815.7	5130.8	24/70
1	0	3	4813.3	5156.1	8/70
0	2	2	4786.2		6/70
0	1	3	4783.6	5105.2	8/70
0	0	4		5130.5	1/70
2	2	1	4743.2		2/28
2	1	2	4740.8	5052.3	6/28
2	0	3	4738.5	5077.3	2/28
1	2	2	4711.4		6/28
1	1	3	4708.9	5026.9	8/28
1	0	4		5051.9	1/28
0	2	3	4679.9		2/28
0	1	4		5001.7	1/28
2	2	2	4636.5		6/28
2	1	3	4634.2	4948.4	8/28
2	0	4		4973.2	1/28
1	2	3	4605.3		8/28
1	1	4		4923.5	4/28
2	2	3	4530.5		2/4
2	1	4		4845.1	1/4

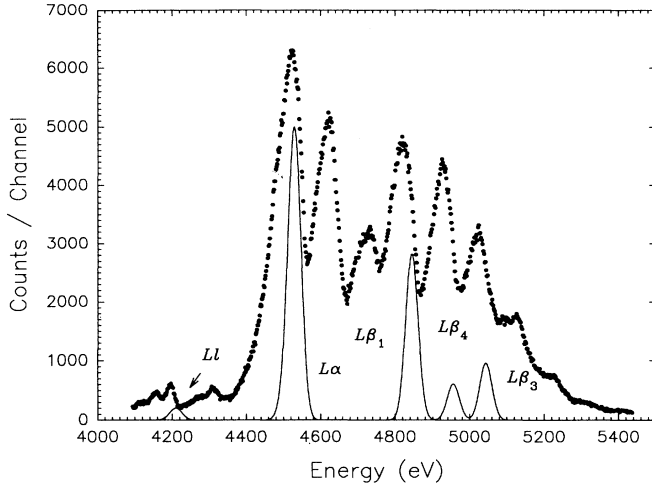


FIG. 5. Comparison of the simulated spectrum for  $n_L=7$  with the 6-MeV/u Xe spectrum obtained with a thick Li target.

rates for single-vacancy atoms. The simulated spectrum for  $n_L=7$  is shown together with a measured spectrum (Li target) in Fig. 5. From this comparison and those for other values of  $n_L$ , it was concluded that the main components present in the measured spectra are  $L\alpha_1$  and  $L\beta_1$  pairs from Xe ions having  $n_L$  from 7 to 4. Additionally, the simulated spectra predicted that the  $L\beta_4$  and  $L\beta_3$  transitions should contribute to the structure at the high-energy end. However, for  $n_L \leq 5$ , the calculations showed that the  $L\beta_4$  peak merges together with the  $L\beta_1$ . The peaks in the simulated spectra were all shifted toward higher energies relative to the peaks in the measured spectra, as may be seen in Fig. 5. This indicates that the x-ray components in the experimental spectrum were emitted from atoms containing (on average) several additional  $M$ -shell (spectator) electrons. It was determined, for a selected number of representative cases, that adding spectator electrons to the  $M$  shell causes all the calculated  $L$  x-ray energies to shift down in energy by an amount  $\Delta E \approx 24$  eV per spectator electron (to within a few eV). Another characteristic revealed by the calculations was that the energy of the  $L\beta_1$  transition in a Xe atom having  $n_L$   $L$ -shell electrons in the initial state is very close to the energy of the  $L\alpha_1$  transition in a Xe atom having  $n_L-3$   $L$ -shell electrons in the initial state when  $n_L \geq 4$ . This helps explain why the peaks in the spectra for low- $Z$  targets were better resolved than first expected.

### C. Charge distribution

The charge distribution of 8-MeV/u Xe ions emerging from carbon foils has been studied recently [43] and both

the equilibrium charge distribution and equilibrium average charge (outside the foil) were found to be closely represented by the semiempirical formulas given by Sayer [44], as well as those of Nikolaev and Dimitriev [45]. In this connection, an intriguing question arises. Can the present  $L$  x-ray spectra be utilized to obtain information pertaining to the charge distributions of ions *inside* solid targets? In an effort to address this question, detailed analyses of the  $L$  x-ray spectra were performed with a customized nonlinear least-squares-fitting program designed to extract the fundamental parameters of the charge distribution. The analytical fitting function employed was based upon the following premises.

(a) During the  $L$  x-ray emission stage, the  $K$  shell remains filled while shells higher than the  $M$  shell are completely stripped of electrons.

(b) The population distribution of the  $L$  shell is described by a Gaussian distribution function having a variable centroid and standard deviation, while the population distribution of the  $M$  shell is described by a binomial distribution.

(c) The  $L$  and  $M$  electrons are statistically distributed among their subshells.

(d) The contributions of all  $L$  x-ray components other than  $L\alpha_1$  and  $L\beta_1$  are small enough to be neglected.

Premise (a) was tested by performing a spectral scan over the projectile  $M$  x-ray region, whereupon it was discovered that the intensities of the  $M$  x-rays were negligible. Premise (b) is based on the statistical nature of the electron ionization and capture processes in high-energy collisions and the fact that many collisions occur prior to  $L$  x-ray emission. The charge distributions resulting from multiple-electron ionization in single collisions are generally well represented by binomial distribution functions. However, analyses performed on the spectra using a binomial  $L$  electron distribution, in general, gave poorer quality fits and values for the other fitting parameters that did not differ significantly from those obtained with a Gaussian  $L$  electron distribution. A statistical distribution of electrons [premise (c)] is reasonable in the absence of preferential population mechanisms. Premise (d) was adopted in order to keep the fitting function as simple as possible and because initial attempts to include the  $L\beta_4$  and  $L\beta_3$  components in the analysis indicated that their contributions were negligible. As may be seen from the simulated spectrum in Fig. 5, these two transitions appear at the high-energy end of the spectrum and have fairly small intensities. Evidently, the actual intensities are substantially less than those predicted by the calculated rates for singly ionized atoms.

The fitting function  $y(E)$  chosen for the spectral analysis was

$$\begin{aligned}
 y(E) = & \sum_{n_{L_1}=0}^2 \sum_{n_{L_2}=0}^2 \sum_{n_{L_3}=0}^4 \sum_{n_M=0}^{18} A(n_L, n_M) P_{n_L}(n_{L_1}, n_{L_2}, n_{L_3}) \\
 & \times \{ (1 - \delta_{n_{L_3}, 4}) \omega_{3d \rightarrow 2p}(n_M) G_\alpha(n_{L_1}, n_{L_2}, n_{L_3}, n_M) \\
 & + \kappa (1 - \delta_{n_{L_2}, 2}) \omega_{3d \rightarrow 2p}(n_M) G_\beta(n_{L_1}, n_{L_2}, n_{L_3}, n_M) \} + B, \quad (1)
 \end{aligned}$$

where

$$A(n_L, n_M) = \frac{A_0}{\sqrt{2\pi}\sigma_L} \exp[-(n_L - n_L^c)^2 / 2\sigma_L^2] \times \binom{18}{n_M} p_M^{n_M} (1 - p_M)^{18 - n_M}, \quad (2)$$

$$P_{n_L}(n_{L_1}, n_{L_2}, n_{L_3}) = \frac{\binom{2}{n_{L_1}} \binom{2}{n_{L_2}} \binom{4}{n_{L_3}}}{\binom{8}{n_L}}, \quad (3)$$

$$G_k(n_{L_1}, n_{L_2}, n_{L_3}, n_M) = \frac{1}{\sqrt{2\pi}\sigma_x} \exp\{-[E - E_k(n_{L_1}, n_{L_2}, n_{L_3}, n_M)]^2 / 2\sigma_x^2\}, \quad (4)$$

and

$$E_k(n_{L_1}, n_{L_2}, n_{L_3}, n_M) = E_k(n_{L_1}, n_{L_2}, n_{L_3}, 1) - (n_M - 1)\Delta E, \quad (5)$$

with  $\Delta E = 24$  eV. The variable parameters of the fitting function are the overall amplitude  $A_0$ , the centroid  $n_L^c$ , and standard deviation  $\sigma_L$  of the initial-state  $L$  electron population distribution, the  $M$ -electron occupation probability  $p_M$ , the standard deviation of the individual x-ray peaks  $\sigma_x$ , the  $L\beta_1$  to  $L\alpha_1$  ratio of the transition rates  $\kappa$ , and the background amplitude  $B$ . The  $P_{n_L}$  factor gives the relative statistical probability that a projectile having

$n_L$  electrons in the initial state assumes a particular configuration. The  $L\alpha_1$  and  $L\beta_1$  transition energies are represented by  $E_\alpha$  and  $E_\beta$ , respectively. The Kronecker delta symbols  $\delta$  in Eq. (1) ensure that the initial configurations having  $n_{L_3} = 4$  for  $L\alpha_1$  transitions and  $n_{L_2} = 2$  for  $L\beta_1$  transitions are excluded from the summations. Although the fitting function contained a large number of peaks, it employed only seven variable parameters.

The fluorescence yields  $\omega_{3d \rightarrow 2p}$  were calculated using the scaling procedure outlined by Larkins [46]. In the present work, it was necessary to estimate the fluorescence yields for  $3d \rightarrow 2p$  transitions in Xe ions having multiple  $M$  vacancies and empty  $N$  and  $O$  shells. Recognizing that for such highly ionized atoms Coster-Kronig processes are energetically forbidden, the fluorescence yields of interest may be expressed as

$$\omega_{3d \rightarrow 2p} = R'(2p, 3d) / R'(\text{tot}), \quad (6)$$

where  $R'(2p, 3d)$  is the radiative rate for a  $3d \rightarrow 2p$  transition in an ion having multiple  $M$ -shell vacancies. According to Larkins, this rate is approximately the rate for atoms having a full  $M$  shell  $R(2p, 3d)$  reduced by the ratio  $(n/n_0)_{3d}$ , where  $n$  is the number of  $3d$  electrons present in the ion and  $n_0$  is the number present in the neutral atom:

$$R'(2p, 3d) = (n/n_0)_{3d} R(2p, 3d). \quad (7)$$

In a similar manner, the total decay rate of a  $2p$  vacancy  $R'(\text{tot})$  may be obtained from the appropriately scaled radiative and Auger rates:

$$\begin{aligned} R'(\text{tot}) = & (n/n_0)_{3d} R(2p, 3d) + (n/n_0)_{3s} R(2p, 3s) + [n(n-1)/n_0(n_0-1)]_{3s} R(2p, 3s, 3s) \\ & + (n/n_0)_{3s} (n/n_0)_{3p} R(2p, 3s, 3p) + (n/n_0)_{3s} (n/n_0)_{3d} R(2p, 3s, 3d) \\ & + [n(n-1)/n_0(n_0-1)]_{3p} R(2p, 3p, 3p) + (n/n_0)_{3p} (n/n_0)_{3d} R(2p, 3p, 3d) \\ & + [n(n-1)/n_0(n_0-1)]_{3d} R(2p, 3d, 3d). \end{aligned} \quad (8)$$

The theoretical radiative rates of Scofield [42] and Auger rates of Walters and Bhalla [47] were used to calculate fluorescence yields for all  $M$ -subshell configurations having  $1 \leq n_M \leq 18$ . Finally, an average fluorescence yield was obtained for each  $n_M$  value by (statistically) averaging the individual fluorescence yields for all contributing configurations. These average fluorescence yields are listed in Table III.

It was discovered that the above fitting function was unable to account for the large tails on the low-energy sides of the spectra obtained with thick targets; nor was it able to reproduce the structure near the centers of the spectra. Both problems caused the program to overestimate the  $n_L = 7$  and 6 contributions as it attempted to compensate for these deficiencies. The overall quality of

TABLE III. Average fluorescence yields for  $3d \rightarrow 2p$  transitions in Xe ions having  $n_M$   $M$ -shell electrons and empty  $N$  and  $O$  shells.

$n_M$	$\omega_{3d \rightarrow 2p}$	$n_M$	$\omega_{3d \rightarrow 2p}$
1	0.556	10	0.179
2	0.581	11	0.164
3	0.470	12	0.152
4	0.384	13	0.141
5	0.323	14	0.132
6	0.278	15	0.123
7	0.245	16	0.116
8	0.218	17	0.110
9	0.196	18	0.104

the fits to the spectra obtained with thin targets, on the other hand, was quite good. The reason for this can be understood by comparing spectra (a), (b), and (c) in Fig. 4. It is readily apparent that the low-energy sides of the spectra for thin targets do not display nearly as much tailing as is present in the spectra for thick targets. The differences between the fits for the spectra obtained with thick and thin carbon targets led to the conclusion that both the  $L\alpha_1$  and the  $L\beta_1$  peaks for  $n_L=7$  in the spectra for thick targets contain asymmetric tails on their low-energy sides. As mentioned earlier, it is suspected that most of this tail arises from x-ray emission beyond the equilibration depth, after the projectile has slowed down significantly and consequently has picked up additional  $M$ -shell electrons.

As a means of accounting for the low-energy tails, the function  $G_k$  [Eq. (4)] was modified for the specific cases where  $n_{L_1} + n_{L_2} + n_{L_3} = 7$  and  $E \leq E_k$  by replacing  $\sigma_x$  in the exponential with  $\sigma'_x$ , a different and independently variable standard deviation, thus bringing the total number of fitting parameters to 8. This procedure allowed the Gaussians representing the  $n_L=7$   $L\alpha_1$  and  $L\beta_1$  components to have larger standard deviations on their left-hand sides than on their right-hand sides. Results of the fitting analysis are shown in Fig. 6 for the 6-MeV/u spectra obtained with thick Li, Be, and C targets. For the sake of clarity, all  $L\alpha_1$  components corresponding to the same value of  $n_L$  are shown as single peaks, and likewise for the  $L\beta_1$  components. Overall, the fitting function reproduced the structure extremely well considering the fact that other low-intensity  $L$  x-ray lines (e.g.,  $L\beta_4$  and  $L\beta_3$ ) probably contribute to the spectra.

The average numbers of projectile  $L$  and  $M$  electrons were determined from the best-fit values of the amplitudes  $A(n_L, n_M)$  using the relationships

$$\bar{n}_{L \text{ or } M} = \frac{\sum_{n_L=0}^8 \sum_{n_M=0}^{18} n_{L \text{ or } M} A(n_L, n_M)}{\sum_{n_L=0}^8 \sum_{n_M=0}^{18} A(n_L, n_M)} \quad (9)$$

and the average projectile charge was obtained from

$$\bar{Q} = \sum_{Q=26}^{52} QY(Q), \quad (10)$$

where the charge yield fractions  $Y(Q)$  were calculated by summing the normalized  $A(n_L, n_M)$  over all combinations for which  $n_L + n_M = 52 - Q$ . It should be noted that the tails on the  $n_L=7$  peaks were not included in the determination of the values of any of the above parameters because these contributions were believed to arise from beyond the equilibration depth.

The numerical results of the spectral analyses are given in Table IV. For 6-MeV/u Xe ions interacting with thick targets, it is found that  $\bar{n}_L$  is essentially independent of the target  $Z$ , except for the case of Be, which displays a

significantly lower  $\bar{n}_L$  than the rest. This latter observation is consistent with the distinctively different character of the spectrum obtained with the Be target, as may be verified by noting the relative contributions of the  $N_L=7-5$   $L\alpha$  peaks in Figs. 2 and 6. The value of  $\bar{n}_M$ , on the other hand, rises steadily from  $Z_2=3$  to 10 (NaF) and remains approximately constant thereafter. As a consequence of this behavior, the average projectile charge decreases by about four units over the  $Z_2$  range 3-10 and remains constant at approximately 40 thereafter. The

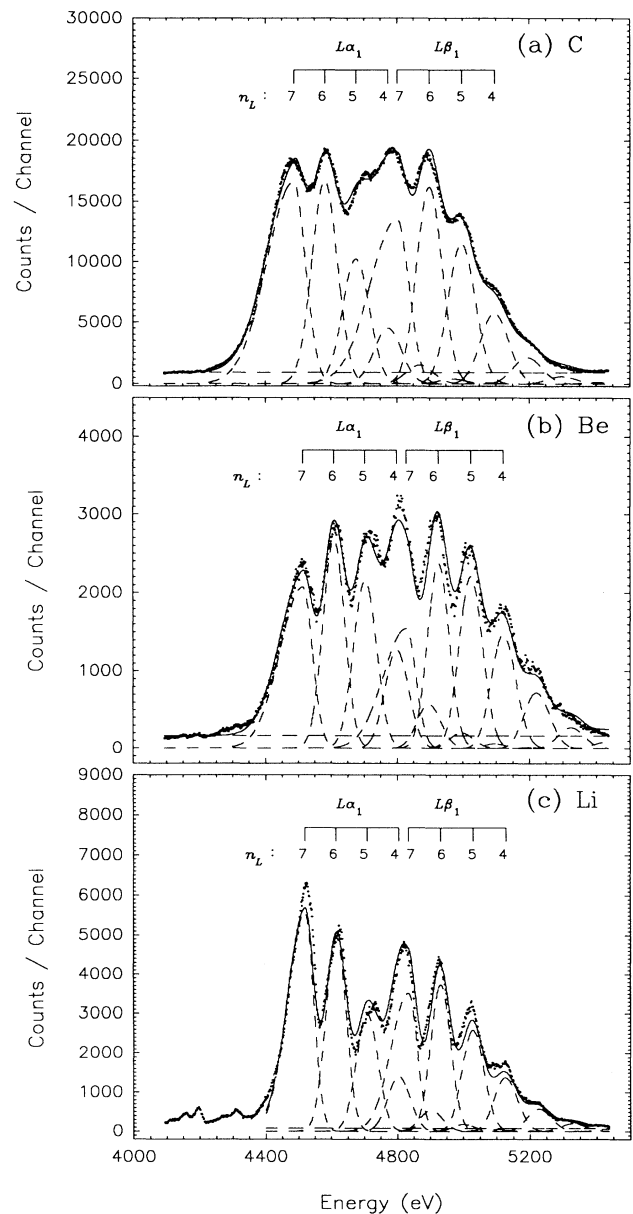


FIG. 6. Least-squares-fitting analysis of 6-MeV/u Xe spectra obtained with thick (a) C, (b) Be, and (c) Li targets. The fitting function is shown by the solid curve, while the composite  $L\alpha_1$  and  $L\beta_1$  components for individual  $n_L$  values are shown by the dashed curves.

TABLE IV. Results of the least-squares-fitting analysis. (The estimated uncertainties are  $\pm 0.4$  for  $\bar{n}_L$  and  $\bar{n}_M$ ,  $\pm 0.6$  for  $\bar{Q}$ ,  $\pm 0.4$  for  $\sigma_L$ ,  $\pm 5$  eV for  $\sigma_x$ ,  $\pm 0.2$  for  $\sigma_Q$ , and  $\pm 0.2$  for  $\kappa$ .)

Projectile energy (MeV/u)	Target <sup>a</sup>	$\bar{n}_L$	$\bar{n}_M$	$\bar{Q}$	$\sigma_L$	$\sigma_x$ (eV)	$\sigma_Q$	$\kappa$
6	Li	6.6	1.2	44.2	2.1	22	1.7	1.3
6	Be	6.0	1.6	44.4	1.9	23	2.0	1.4
6	B	6.6	3.4	42.0	1.8	25	2.1	1.6
6	C	6.5	3.5	42.0	1.8	26	2.1	1.6
6	BN	6.6	3.9	41.5	1.7	27	2.2	1.6
6	NaF	6.6	5.9	39.5	1.7	23	2.3	1.5
6	Al	6.5	5.7	39.8	1.6	20	2.3	1.8
6	KCl	6.5	5.5	40.0	1.4	18	2.3	1.9
6	C(100)	6.4	2.9	42.7	1.7	19	2.0	1.3
6	C(200)	5.9	2.9	43.2	1.6	19	2.1	1.3
8	C(200)	4.9	2.8	44.3	1.8	13	2.3	1.1
8	C(200) <sup>b</sup>	4.5	2.8	44.7	1.6	12	2.2	1.3
8	Al(150)	5.4	4.6	42.0	1.6	19	2.4	1.3
8	Ni(180)	5.9	4.5	41.6	1.7	15	2.3	1.5

<sup>a</sup>For thin targets, the nominal thickness ( $\mu\text{g}/\text{cm}^2$ ) is given in parentheses.

<sup>b</sup>This target was preceded by a  $200\text{-}\mu\text{g}/\text{cm}^2$  C stripper foil.

same behavior is observed for  $\bar{Q}$  at 8 MeV/u in that it also decreases by about three units as  $Z_2$  increases from 6 to 28, although it is caused, in this case, by an increase in both  $\bar{n}_L$  and  $\bar{n}_M$ . In comparing the results presented in Table IV with the spectra displayed in Fig. 2, it is evident that the disappearance of resolved x ray structure as  $Z_2$  increases coincides with the increase in  $\bar{n}_M$ . Moreover,  $\bar{n}_M$  closely correlates with the average electron density of the target.

The predicted equilibrium charge of 6-MeV/u Xe ions after exiting a carbon foil is 42.7 [44], which is very close to the average for the three carbon targets. The predicted value of the equilibrium charge at 8 MeV/u (44.8) is also nearly the same as the  $\bar{Q}$  deduced from the spectra obtained with  $200\text{-}\mu\text{g}/\text{cm}^2$  C targets.

The charge distribution widths  $\sigma_Q$  listed in Table IV were calculated using the relation

$$\sigma_Q = \left[ \sum_{Q=35}^{52} (Q - \bar{Q})^2 Y(Q) \right]^{1/2}. \quad (11)$$

The values of  $\sigma_Q$  for the carbon targets range from 1.7 to 2.4 and compare quite favorably with the value of 1.8 predicted for the equilibrium charge distribution in carbon [44].

The  $L\beta_1$ -to- $L\alpha_1$  transition rate ratio  $\kappa$  was found to range from 1.1 to 1.9 (see Table IV). The value of this ratio predicted by theoretical transition rates for singly ionized Xe atoms is 1.2 [42]. Comparing the 6-MeV/u-thick target ratios, divided by 2 to convert from transition rate ratio to intensity ratio, with the data displayed in Fig. 6.17 of Ref. [48], it is noted that the present results rise fairly monotonically from 0.65 at  $Z_2=3$  and smoothly join the 5.9-MeV/u Xe data of Folkmann and Mokler [49] at  $Z_2=13$ . At these high projectile energies, the oscillatory  $Z_2$  dependence of the  $L\beta$ -to- $L\alpha$  intensity ratio that is so prominent at energies below  $\sim 1$  MeV/u has completely disappeared. This is to be expected since the

oscillatory behavior has been attributed to a molecular-orbital electron promotion mechanism [26], whereas in the high-energy regime of the present measurements, direct Coulomb ionization is expected to be the predominant mechanism involved.

Finally, it is noted that the  $\sigma_x$  values obtained for the x-ray peaks are considerably larger than the 7.4-eV limit imposed by the spectrometer resolution. A possible cause of this apparent peak broadening is the underlying multiplet structure associated with the angular momentum coupling of the multiple  $L$  and  $M$  vacancies. The observed x-ray peak widths are reasonably consistent with estimates of the magnitude of this effect by Hagmann *et al.* [25]. However, the thin target spectra appear to have smaller x-ray peak widths than the thick target spectra and the x-ray peak widths for the 8-MeV/u spectra are substantially smaller than those for the 6-MeV/u spectra. These observations suggest that another broadening mechanism contributes to the peak widths.

The present results indicate that the average (equilibrium) charges for 6- and 8-MeV/u Xe ions are nearly the same inside and outside a carbon target. At first sight, this conclusion appears to be contrary to the usual expectation that the charge outside the target should be larger than the charge inside because of the occurrence of Auger relaxation after the projectile exits from the foil [50,51]. Each decay of this type would increase  $Q$  by one unit. However, for the high states of ionization involved in the cases under consideration here, the projectile is so devoid of outer-shell electrons ( $\bar{n}_M \approx 2.9$  for the thin carbon targets) that Auger decay is greatly suppressed and hence the charge should not increase very much after the ion exits a thin carbon foil. In order to test this hypothesis, the population distribution deduced from the  $L$  x-ray spectrum obtained at 8 MeV/u with a  $200\text{-}\mu\text{g}/\text{cm}^2$  carbon foil was used to predict the final charge distribution after deexcitation outside the target. This was accomplished by apportioning the yield for each electron

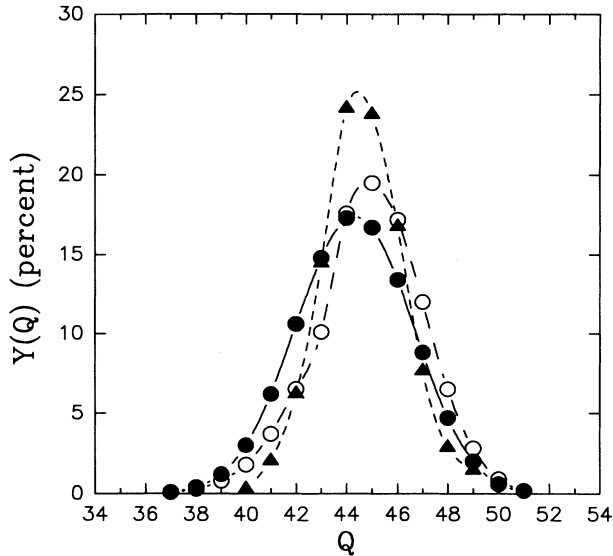


FIG. 7. Comparison of charge distributions for 8-MeV/u Xe ions in carbon. Filled circles, charge distribution inside the target deduced from the  $L$  x-ray measurements; open circles, predicted charge distribution outside the target; filled triangles, charge distribution outside the target measured by magnetic charge state analysis [43].

configuration between its Auger and x-ray decay branches at each step of the deexcitation process until its final configuration (with either  $n_L=8$  or  $n_M=0$ ) was reached. These calculations revealed that the centroid of the final charge distribution is shifted up in charge by only 0.5 units from that of the original charge distribution. The charge distribution inside the target deduced from the x-ray measurements, the predicted charge distribution outside the target, and the charge distribution determined by magnetic charge state analysis of 8-MeV/u Xe ions emerging from a  $300\text{-}\mu\text{g}/\text{cm}^2$  carbon foil [43] are compared in Fig. 7. It is evident that the centroids of the two "outside" charge distributions agree within experimental error, but that the predicted charge distribution has a somewhat larger width than the measured charge distribution.

#### IV. CONCLUSION

The structure of the Xe projectile  $L$  x-ray spectra displayed a strong dependence on the target atomic number. Spectra obtained with low- $Z_2$  targets were charac-

terized by partially resolved peaks which broadened and merged together as the target atomic number was increased beyond  $Z_2=6$ . Moreover, the energies of the principal spectral components systematically decreased as  $Z_2$  increased. The overall spectral shape changed and its position shifted to higher energy when the projectile energy was changed from 6 to 8 MeV/u, in response to the shift in the equilibrium charge distribution. The spectra obtained with thick and thin carbon targets were remarkably similar, with the only significant differences appearing in the low-energy tail region.

The main components of the spectra were identified to be  $L\alpha_1$  and  $L\beta_1$  pairs from projectile initial states having one to four  $L$ -shell vacancies. From comparisons of the spectra obtained with both thick and thin targets, it was concluded that the  $L$  x-ray structure closely mirrors the equilibrium charge distribution at 6 and 8 MeV/u. This rather unique circumstance is a consequence of the fact that, at these velocities, the existence of at least one  $L$ -shell vacancy is highly probable in a charge-equilibrated Xe ion, while the existence of a  $K$  shell vacancy is relatively improbable.

Detailed spectral analysis enabled extraction of fundamental parameters which characterized the  $L$ - and  $M$ -shell population distributions as well as the charge distributions of the projectile ions inside the solid targets. The results revealed that the observed structural evolution in the x-ray spectra with increasing  $Z_2$  is caused primarily by the correlation between  $\bar{n}_M$  (and its associated distribution width) and the average electron density of the target. In addition it was found that at 6 and 8 MeV/u, the average projectile (equilibrium) charges inside and outside a carbon target are nearly the same. The values of the average equilibrium charges and the widths of the charge distributions deduced from the x-ray spectra obtained with carbon targets were in good agreement with tested semiempirical predictions and, in the case of the 8-MeV/u data, with the results of magnetic charge state analysis. This work has demonstrated that under suitable conditions, highly detailed and reliable information about the charge distributions of ions traveling in solids may be obtained from x-ray measurements.

#### ACKNOWLEDGMENTS

This work was supported by the Division of Chemical Sciences, Office of Basic Energy Sciences, U.S. Department of Energy, and by the Robert A. Welch Foundation.

- [1] C. F. Moore, H. H. Wolter, R. L. Kaufman, J. McWhorter, J. E. Bolger, and C. P. Browne, *J. Phys. B* **5**, L262 (1972).
- [2] A. R. Knudson, P. G. Burkhalter, and D. J. Nagel, in *Atomic Collisions in Solids*, edited by S. Datz, B. R. Appelt, and C. D. Moak (Plenum, New York, 1975), Vol. 1, p. 421.
- [3] R. L. Watson, J. R. White, and F. E. Jenson, *Phys. Lett.* **67A**, 269 (1978).

- [4] R. L. Watson, J. R. White, A. Langenberg, R. A. Kenefick, and C. C. Bahr, *Phys. Rev. A* **22**, 582 (1980).
- [5] R. J. Maurer, R. L. Watson, O. Benka, J. M. Sanders, and D. M. Oldham, *Nucl. Instrum. Methods* **202**, 193 (1982).
- [6] R. J. Maurer, R. L. Watson, and G. J. Pedrazzini, *Nucl. Instrum. Methods* **214**, 117 (1983).
- [7] H. D. Betz, F. Bell, H. Panke, G. Kalkoffen, M. Welz, and D. Evers, *Phys. Rev. Lett.* **33**, 807 (1974).
- [8] H. Panke, F. Bell, H.-D. Betz, W. Stehling, E. Spindler,

- and R. Laubert, *Phys. Lett.* **53A**, 457 (1975).
- [9] H. Panke, F. Bell, H.-D. Betz, and W. Stehling, *Nucl. Instrum. Methods* **132**, 25 (1976).
- [10] P. Nikolai, M. Chabot, J. P. Rozet, M. F. Politis, A. Chetioui, C. Stephan, A. Touati, D. Vernhet, and K. Wohrer, *J. Phys. B* **23**, 3609 (1990).
- [11] J. P. Rozet, A. Chetioui, P. Nikolai, M. Chabot, M. F. Politis, A. Touati, D. Vernhet, K. Wohrer, C. Stephan, and J. P. Grandin, *Z. Phys. D* **21S**, 331 (1991).
- [12] F. Bell, H.-D. Betz, H. Panke, W. Stehling, and E. Spindler, *J. Phys. B* **9**, 3017 (1976).
- [13] R. J. Fortner and D. L. Matthews, *Phys. Rev. A* **16**, 1441 (1977).
- [14] J. P. Rozet, A. Chetioui, P. Bouisset, D. Vernhet, K. Wohrer, and A. Touati, *Phys. Rev. Lett.* **58**, 337 (1987).
- [15] K. Shima, K. Umetani, and T. Mikumo, *Nucl. Instrum. Methods* **194**, 353 (1982).
- [16] T. Mizogawa, Y. Awaya, T. Kambara, Y. Kanai, M. Kase, H. Kumagai, P. H. Mokler, and K. Shima, *Nucl. Instrum. Methods A* **262**, 141 (1987).
- [17] T. Mizogawa, Y. Awaya, T. Kambara, Y. Kanai, M. Kase, H. Kumagai, P. H. Mokler, and K. Shima, *Phys. Rev. A* **42**, 1275 (1990).
- [18] R. C. Der, R. J. Fortner, T. M. Kavanah, and J. D. Garcia, *Phys. Rev. Lett.* **27**, 1631 (1971).
- [19] H. Panke and F. Bell, *Phys. Lett.* **43A**, 351 (1973).
- [20] R. J. Fortner, *Phys. Rev. A* **10**, 2218 (1974).
- [21] R. J. Fortner, D. L. Matthews, and J. H. Scofield, *Phys. Lett.* **53A**, 336 (1975); R. J. Fortner, D. L. Matthews, and J. D. Garcia, *ibid.* **53A**, 464 (1975).
- [22] R. J. Fortner and J. D. Garcia, in *Atomic Collisions in Solids* (Ref. [2]), p. 469.
- [23] T. M. Kavanagh, R. C. Der, R. J. Fortner, and M. E. Cunningham, *Phys. Rev. A* **8**, 2322 (1973); R. J. Fortner and J. D. Garcia, *ibid.* **12**, 856 (1975).
- [24] S. Datz, C. D. Moak, B. R. Appelton, and T. A. Carlson, *Phys. Rev. Lett.* **27**, 363 (1971).
- [25] S. Hagmann, P. Armbruster, G. Kraft, P. H. Mokler, and H.-J. Stein, *Z. Phys. A* **288**, 353 (1978).
- [26] S. Hagmann, P. Armbruster, G. Kraft, P. H. Mokler, and H.-J. Stein, *Z. Phys. A* **290**, 25 (1979).
- [27] S. Datz, *Nucl. Instrum. Methods* **132**, 7 (1976).
- [28] D. K. Olsen, C. F. Moore, and P. Richard, *Phys. Rev. A* **7**, 1244 (1973).
- [29] R. L. Watson, A. Langenberg, R. A. Kenefick, C. C. Bahr, and J. R. White, *Phys. Rev. A* **23**, 2471 (1981).
- [30] A. R. Knudson, P. G. Burkhalter, and D. J. Nagel, *Phys. Rev. A* **10**, 2118 (1974).
- [31] R. J. Fortner, D. L. Matthews, J. D. Garcia, and H. Oona, *Phys. Rev. A* **14**, 1020 (1976).
- [32] F. Bell, H.-D. Betz, H. Panke, and W. Stehling, *J. Phys. B* **9**, L443 (1976).
- [33] G. J. Pedrazzini, J. Palinkas, R. L. Watson, D. A. Church, and R. A. Kenefick, *Nucl. Instrum. Methods B* **10/11**, 904 (1985).
- [34] The Nucleus Inc., 761 Emory Valley Road, Oak Ridge, TN 37830.
- [35] F. Hubert, R. Bimbot, and H. Gauvin, *At. Data Nucl. Data Tables* **46**, 1 (1990).
- [36] Y. Baudinet-Robinet, *Nucl. Instrum. Methods* **190**, 197 (1981).
- [37] J. A. Bearden, *Rev. Mod. Phys.* **39**, 78 (1967).
- [38] W. H. McMaster, N. K. Del Grande, I. H. Mallet, and J. H. Hubell, Lawrence Livermore National Laboratory Report No. UCRL-50174, Sec. II, Rev. 1, 1969 (unpublished).
- [39] E. J. McGuire, *Phys. Rev. A* **3**, 587 (1971).
- [40] F. Hopkins, in *Methods of Experimental Physics*, edited by P. Richard (Academic, New York, 1980), Vol. 17, p. 355.
- [41] J. P. Desclaux, *Comput. Phys. Commun.* **9**, 31 (1975).
- [42] J. H. Scofield, *At. Data Nucl. Data Tables* **14**, 122 (1974).
- [43] R. L. Watson, V. Horvat, R. Parameswaran, L. Cook, J. Knott, and A. Nash (unpublished).
- [44] R. O. Sayer, *Rev. Phys. Appl.* **12**, 1543 (1977).
- [45] V. S. Nikolaev and I. S. Dimitriev, *Phys. Lett.* **28A**, 277 (1968).
- [46] F. P. Larkins, *J. Phys. B* **4**, L29 (1971).
- [47] D. L. Walters and C. P. Bhalla, *Phys. Rev. A* **4**, 2164 (1971).
- [48] P. H. Mokler and F. Folkmann, in *Structures and Collisions of Ions and Atoms*, edited by I. Sellin and L. Armstrong, Topics in Current Physics Vol. 5 (Springer-Verlag, Berlin 1978), p. 201.
- [49] F. Folkmann and P. H. Mokler (unpublished).
- [50] H. D. Betz and L. Grodzins, *Phys. Rev. Lett.* **25**, 211 (1970).
- [51] S. Della-Negra, Y. Le Beyec, B. Monart, and K. Standing, *Phys. Rev. Lett.* **58**, 17 (1987).